

Tribovoltaic Effect at Liquid–MoS₂ Interfaces and Spectral Analysis of Interfacial Charge Transfer

Yaxuan Xie, Qingzhang You, Wenjing Bo, Tao Jiang, Mingli Zheng, Peijie Wang,*
Xi Liang,* and Zhong Lin Wang*

Liquid–solid triboelectric nanogenerators (TEENGs) offer a viable approach for harvesting water energy to power Internet of Things systems. Semiconductor-based TEENGs leveraging the tribovoltaic effect have recently emerged as a focus of research. In this paper, monolayer molybdenum disulfide (ML-MoS₂) is introduced as a contacting material for fabricating direct current (DC) liquid–solid nanogenerators. At the internal liquid–solid interface, electron transfer is strongly evidenced by Raman and photoluminescence spectra. For the external characteristics, macroscopic DC outputs are assessed under various conditions, with a maximum current density of 11.1 mA m⁻². Correlating external output patterns with interfacial charge dynamics, a complete working mechanism of the liquid–solid tribovoltaic effect is better elucidated. This work advances innovative strategies for water energy harvesting, deepening fundamental insights into liquid–solid interactions and the tribovoltaic effect.

1. Introduction

Harvesting aquatic energy from diverse sources including river/ocean waves, tidal movements, and rainfall precipitation plays a pivotal role in establishing self-powered aquatic Internet of Things (IoT) networks.^[1–5] Building upon the foundational work by Wang's group,^[6,7] recent advancements in triboelectric nanogenerators (TEENGs) based on liquid–solid contact electrification (CE) have exhibited remarkable capabilities in water energy harvesting.^[8–13] Current research demonstrates that the mechanical-to-electrical energy conversion efficiency of these systems has achieved 11%.^[9,14–16] Nevertheless, conventional liquid–solid TEENGs employing insulating polymer films (e.g., polydimethylsiloxane [PDMS], polytetrafluoroethylene [PTFE], fluorinated ethylene propylene [FEP]) as

tribomaterials inherently produce alternating current (AC) outputs.^[8,17–19] This operational characteristic creates a critical mismatch with the direct current (DC) requirements of most electronic applications, necessitating AC–DC conversion that incurs substantial energy losses.^[20–22]

Unlike traditional TEENGs, CE at semiconductor interfaces demonstrates distinctive DC output behavior, termed the tribovoltaic effect by Wang's group.^[23–25] Notably, emerging research indicates this phenomenon not only manifests at solid–solid interfaces but has been extended to liquid–solid interaction systems.^[26,27] During the contact between a liquid and a semiconductor, electron–hole pairs are excited at the interface region owing to the energy released by the newly formed bonds, which can be named as “bindington.”^[24,28,29] The electron–hole pairs are further driven by the built-in electric field to move from one side to the other side at the interfaces, generating a direct current. This is the tribovoltaic effect, which is analogous to the photovoltaic effect except the excitation photon comes from the energy of bindington.^[24]

Recent studies have validated the tribovoltaic effect between water droplets and silicon substrates, establishing the operational viability of DC liquid–solid nanogenerators.^[26–29] Nevertheless, current implementations remain restricted to silicon-based materials, where their intrinsic material characteristics impede mechanistic investigations of the tribovoltaic effect. Existing methodologies predominantly concentrate on external circuit signal characterization,^[30–32] yet lack direct analytical ap-

Y. Xie, Q. You, W. Bo, P. Wang, X. Liang
Beijing Key Laboratory for Nano-Photonics and Nano-Structure
Department of Physics
Capital Normal University
Beijing 100048, P. R. China
E-mail: pjwang@cnu.edu.cn; liangxi0307@cnu.edu.cn

T. Jiang, Z. L. Wang
Beijing Key Laboratory of Micro-Nano Energy and Sensor
Center for High-Entropy Energy and Systems
Beijing Institute of Nanoenergy and Nanosystems
Chinese Academy of Sciences
Beijing 101400, P. R. China
E-mail: zhong.wang@mse.gatech.edu

Q. You
School of Science
Inner Mongolia University of Science and Technology
Baotou 014010, P. R. China

M. Zheng
Key Lab for Special Functional Materials
Ministry of Education
National and Local Joint Engineering Research Center for High-efficiency
Display and Lighting Technology
School of Nanoscience and Materials Engineering
Collaborative Innovation Center of Nano Functional Materials and Applications
Henan University
Kaifeng 475004, P. R. China

The ORCID identification number(s) for the author(s) of this article can be found under <https://doi.org/10.1002/adma.202506186>

DOI: 10.1002/adma.202506186

proaches for probing interfacial charge dynamics at liquid–solid interfaces. This critical knowledge gap underscores the necessity for developing an in situ charge monitoring technique to advance fundamental understanding of the liquid–solid tribovoltaic mechanism.

In contrast to silicon-based systems, two-dimensional (2D) semiconductor materials demonstrate distinctive physicochemical properties,^[33,34] unveiling novel research opportunities in tribovoltaic effect exploration.^[24] Crucially, monolayer molybdenum disulfide (ML-MoS₂) emerges as a prototypical 2D semiconductor candidate,^[35,36] possessing an N-type semiconducting character with direct bandgap configuration.^[37,38] The implementation of ML-MoS₂ in tribovoltaic systems promises to advance mechanistic studies through its unique optoelectronic signatures.^[39–42] Specifically, ML-MoS₂ exhibits two distinctive Raman-active modes (E¹_{2g} and A¹_{1g}), with the A¹_{1g} vibration mode demonstrating pronounced electron concentration-dependent shifts.^[39,40] Moreover, its photoluminescence (PL) spectrum is dominated by A and A⁻ exciton peaks, both exhibiting carrier density-modulated spectral responses.^[40,42] These inherent spectral-carrier correlations provide a theoretical foundation for developing in situ optical probes to monitor interfacial charge dynamics at liquid–solid tribovoltaic interfaces.

This study pioneers the application of 2D semiconductor ML-MoS₂ as a tribovoltaic interface in DC liquid-solid nanogenerators. Through controlled sliding experiments of deionized (DI) water droplets on the ML-MoS₂ surface, we observe characteristic DC electrical outputs that unambiguously confirm the activation of the tribovoltaic effect. Subsequently, advanced spectroscopic characterization reveals interfacial charge transfer mechanisms via systematic analysis of Raman spectral modifications (A¹_{1g} mode shifts) and PL exciton peak evolution (A⁻/A intensity variations), providing direct experimental evidence of electron transfer at liquid–solid interfaces. The charge transfer direction exhibits strict consistency with external circuit polarity, thereby elucidating the fundamental working principle of the tribovoltaic effect. In addition, molecular dynamics (MD) simulations further uncover molecular-level liquid–solid interaction details. Ultimately, systematic investigation of various liquids establishes quantitative correlations between solution properties and output performance. This work not only develops an in situ spectroscopic methodology for probing liquid–solid interfaces but also provides critical insights for designing high-efficiency water energy harvesters, advancing both fundamental understanding and practical applications of the liquid–solid tribovoltaic effect.

2. Results and Discussion

2.1. Structural and Material Characteristics of the Water-MoS₂ Nanogenerator

Figure 1a schematically illustrates a water droplet sliding on a ML-MoS₂ surface, which functions as the triboelectric layer in the nanogenerator. The ML-MoS₂ film, synthesized via chemical vapor deposition (CVD), exhibits a single-atom-layer thickness and macroscopic dimensions (1 cm × 1 cm). This large-area continuous film was transferred onto a copper (Cu) back electrode sup-

ported by a silicon wafer (1.5 cm × 1 cm), collectively constituting a nanogenerator device (photograph in **Figure S1**, Supporting Information). Device fabrication intentionally designed the ML-MoS₂ film slightly smaller than underlying components to accommodate electrical connections. The scanning electron microscope (SEM) images in **Figure 1b** reveals the distinct boundary between the ML-MoS₂ film and the Cu electrode. The right part of **Figure 1b** verifies a homogeneous distribution of Mo and S elements in the MoS₂ region. In **Figure S2a,b** (Supporting Information), the thickness of the ML-MoS₂ film is confirmed to be 0.734 nm by atomic force microscopy (AFM), confirming the film is a single atomic layer. **Figure S2c,d** (Supporting Information) reveals that the ML-MoS₂ surface is nearly defect-free and clean, with low roughness of only 4.8 nm. In addition, the hydrophilic nature of ML-MoS₂, evidenced by contact angle measurements with DI water (**Figure S3**, Supporting Information), promotes strong interfacial interactions.

The optical features of ML-MoS₂ were analyzed through Raman and PL spectroscopies using a 532 nm continuous laser. As shown in **Figure 1c**, two characteristic Raman peaks were observed: the in-plane vibration mode (E¹_{2g}) at ≈ 383.52 cm⁻¹ and the out-of-plane vibration mode (A¹_{1g}) at around 403.92 cm⁻¹. The peak separation is ≈ 20 cm⁻¹, consistent with standard ML-MoS₂, so confirming its single-layer structure. The PL spectrum (**Figure 1d**) exhibits two prominent peaks at 620 nm (2.00 eV) and 667 nm (1.86 eV). This is attributed to strong intrinsic spin–orbit coupling of ML-MoS₂, and its valence band splits into two states. In the PL spectrum, these two states are observed as the A exciton and B exciton, respectively. The A exciton further interacts with an electron to form the A⁻ trion, leading to a total of three distinct exciton states. Furthermore, ultraviolet–visible (UV) absorption spectroscopy (**Figure 1e**) determines the optical bandgap of ML-MoS₂ to be 1.82 eV, with the original absorption spectrum and the modified Tauc plot calculation methodology provided in **Figure S4** and **Note S1** (Supporting Information) in details.^[43] The calculated result is consistent with previously reported value of ML-MoS₂ ranging from 1.8 to 1.9 eV.^[37] Note that this value obtained here represents the optical bandgap, rather than the intrinsic electronic bandgap, as the latter is higher due to the exciton binding energy. In addition, differences in the energy band structures of single-layer to multi-layer MoS₂ are also discussed in **Note S1** (Supporting Information).

2.2. Typical Output Characteristics in the External Circuit

To investigate the dynamic electrical output behavior during liquid–solid interactions, a microinjector-controlled DI water droplet was positioned above the ML-MoS₂ surface, without direct contact between the conductive needle tip and the material. The circuit diagram for connecting to the electrometer is shown in **Figure S5** (Supporting Information). The current flow through the external circuit, from the needle to the back electrode underneath ML-MoS₂, is defined as the positive direction. Each operational cycle involves droplet volume expansion via water injection, temporary stabilization, and subsequent volume reduction, thereby establishing a controllable friction interface between the droplet and the ML-MoS₂ film, as documented in **Video S1** (Supporting Information).

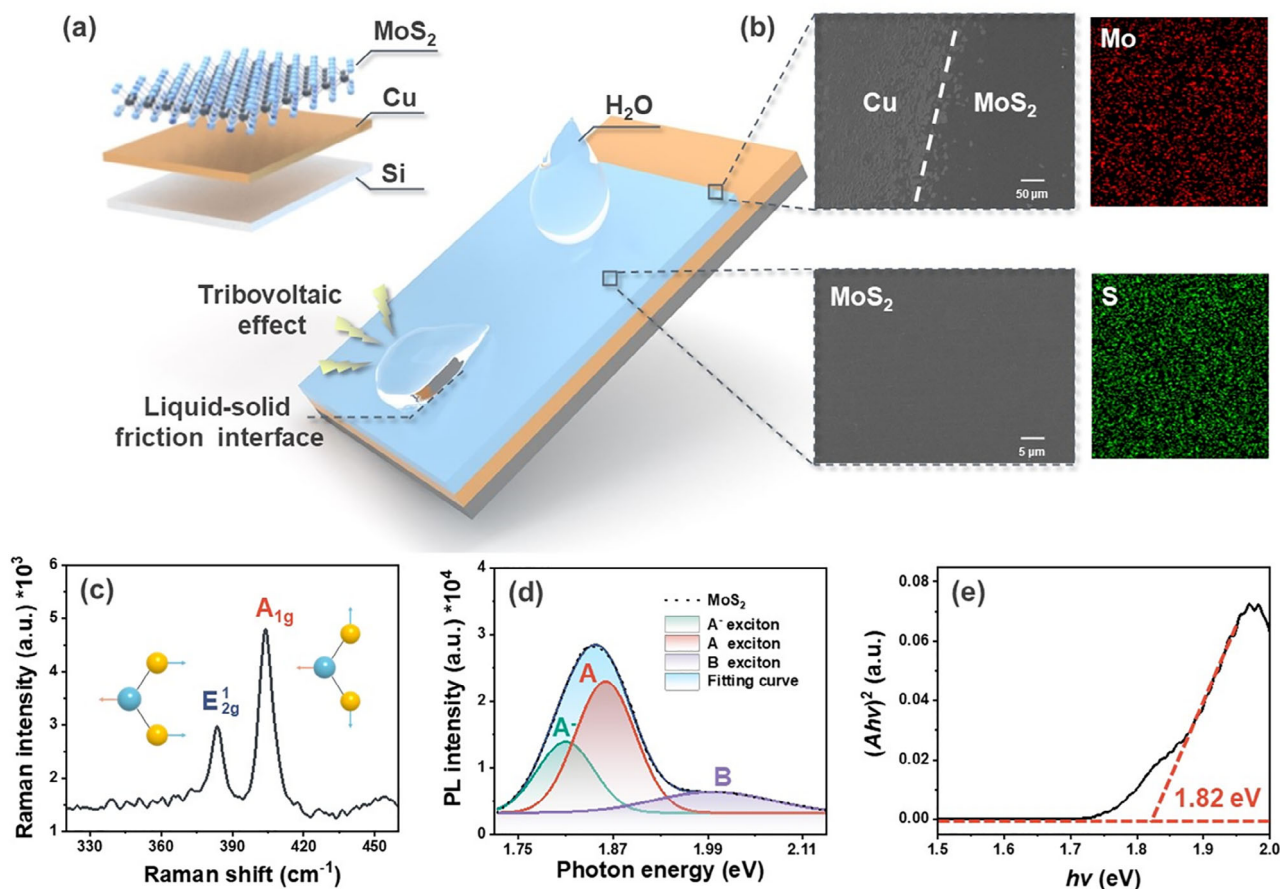


Figure 1. a) Exploded view of the liquid–solid nanogenerator structure based on ML-MoS₂. b) SEM images showing the surface morphology of MoS₂ and Cu, and the elemental mapping analysis of Mo and S. c) Raman spectrum of ML-MoS₂, highlighting characteristic peaks. d) PL spectrum of ML-MoS₂, illustrating its optical properties. e) Plot of $(Ah\nu)^2$ versus $h\nu$ for ML-MoS₂ bandgap determination.

Electrical output measurements during droplet manipulation reveal distinct current responses corresponding to interfacial dynamics. As depicted in **Figure 2a**, during droplet expansion and outward sliding, a positive current peak of ≈ 20 nA occurs. Once the droplet remains stationary at the maximum volume (**Figure 2b**), the current diminishes to baseline, implying cessation of charge flow. A second positive current peak emerges during droplet contraction and inward motion (**Figure 2c**). Full-cycle output characteristics (output voltage, output current, and transferred charge) are detailed in **Figure S6** (Supporting Information). The observation (when droplet movement stops, the output disappears; when the same droplet resumes movement, the output peak reappears) strongly contradicts the hypothesis rooted in electrochemical mechanisms, suggesting that the power generation system relies on liquid–solid movement rather than electrochemistry reactions. Evaporation indeed serves as a means to form a dynamic liquid–solid interface. In order to minimize variables, these experiments were conducted in a high humidity environment ($>50\%$), thereby emphasizing the importance of external mechanical effects. Notably, regardless of sliding directions, the positive external current (from the droplet to the back electrode) persists. This DC result aligns with tribovoltaic effect signatures, which is distinctly

different from ion adsorption or electric double-layer (EDL) mechanisms.

Furthermore, interfacial electrical characterization was conducted through the current–voltage (I – V) measurements between a stationary DI water droplet and the ML-MoS₂ film, with the test configuration illustrated in **Figure S7a** (Supporting Information). The I – V curve (**Figure S7b**, Supporting Information) demonstrates pronounced rectification behavior at the water–MoS₂ interface, analogous to solid-state P–N junctions. This phenomenon arises from the Fermi level disparity between water (acting as a P-type semiconductor analog) and ML-MoS₂ (an N-type semiconductor), driving electron diffusion and establishing a built-in electric field oriented from MoS₂ to water. The direction of this intrinsic field aligns with the positive current observed in external circuits during droplet motion (**Figure S6a**, Supporting Information), corroborating the tribovoltaic mechanism governing charge transfer dynamics in this system. Unlike water, common organic liquids lack the semiconductor properties. We attempted to substitute with alcohol as an alternative medium. The corresponding output performance is illustrated in **Figure S8** (Supporting Information). As demonstrated by the results, alcohol proves to be ineffective as a liquid friction material under these conditions.

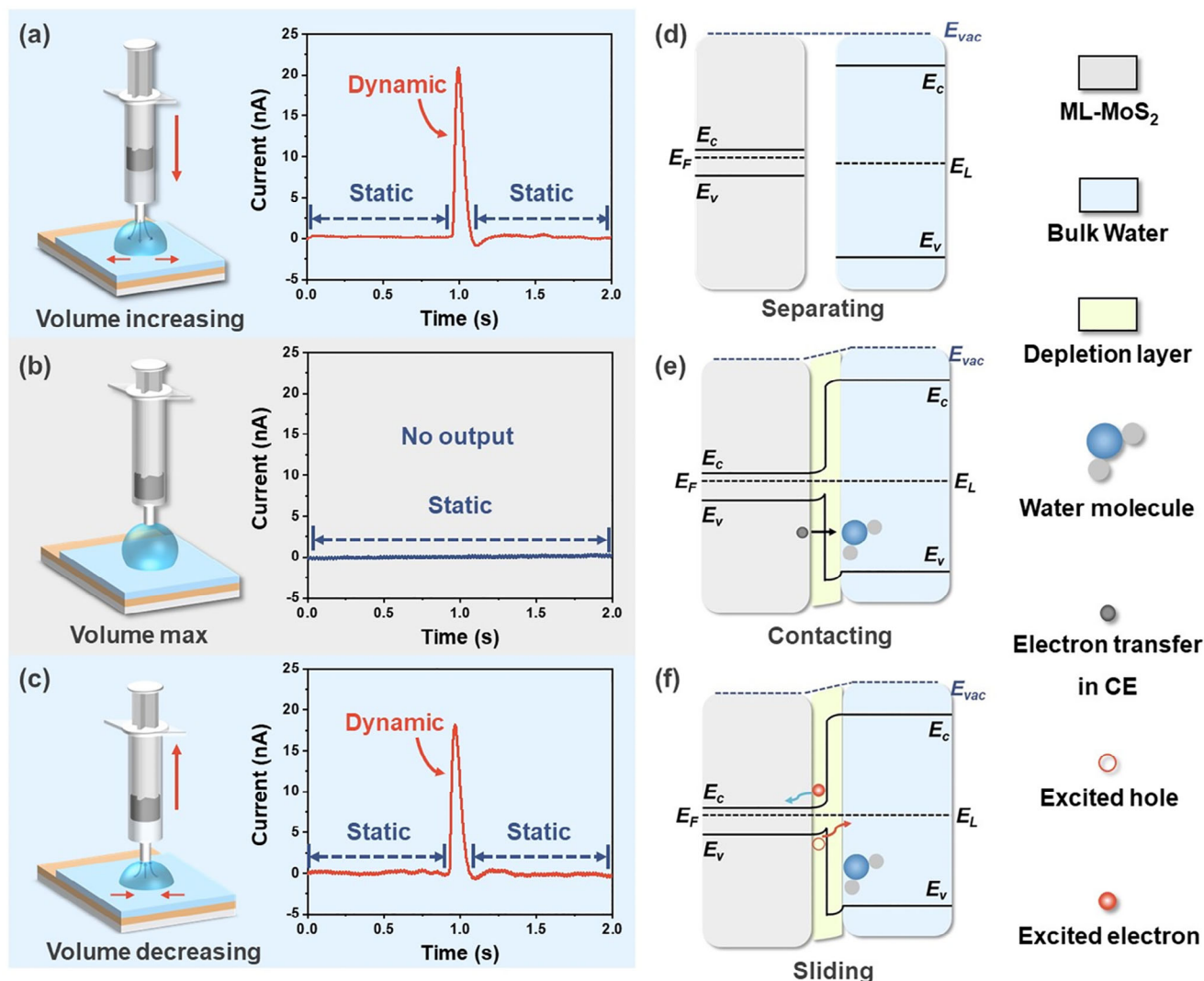


Figure 2. a–c) Output current as the droplet volume increases, at the maximum volume, and as the volume decreases, respectively. Energy band diagrams illustrating the tribovoltaic effect at the liquid–solid interface: d) energy band configuration of MoS₂ and DI water before contact; e) energy band alignment during contact; f) charge movement at the liquid–solid interface during sliding, showing electron and hole dynamics. (E_c represents the conduction band minimum, E_f is the Fermi level of MoS₂, E_v represents the valence band maximum, and E_L is the “Fermi level” of DI water.)

Based on these experiments, the working mechanism of the water–MoS₂ tribovoltaic effect is elucidated through band analysis (Figure 2d–f). Prior to contact (Figure 2d), the Fermi level of ML–MoS₂ exceeds that of DI water. Upon interfacial CE, Fermi-level equilibration drives electron transfer from MoS₂ to water, establishing a built-in electric field oriented from MoS₂ to water (Figure 2e). During dynamic sliding, energy release (bonding) at the interface, attributed to bond breaking and lattice vibrations,^[24] excites electron–hole pairs, as illustrated in Figure 2f. These electron–hole pairs are subsequently separated by the built-in electric field: holes move from the interface toward the water side, while the electrons move to the MoS₂ side, resulting in the positive current (from water to MoS₂) measured in the external circuit. It is important to note that the direction of the built-in electric field is the primary determinant of the external current direction, while other factors, such as droplet movement,

droplet area, or device hysteresis, are irrelevant in this context. This tribovoltaic effect mechanism aligns with the observed DC current in this system and distinguishes it from conventional interfacial charging phenomena.

2.3. Spectral Analysis of Interfacial Electron Transfer

Building upon macroscopic tribovoltaic characterization, this study extends to interfacial charge transfer mechanisms at the liquid–solid interface. While prior works categorize triboelectric charge origins into ion, electron, or material fragment transfer,^[44,45] we pioneer the application of in situ spectroscopic probing to directly resolve interfacial charge dynamics. As schematized in Figure 3a, the fixed laser focal position on the ML–MoS₂ surface ensures spatial consistency across measurements,

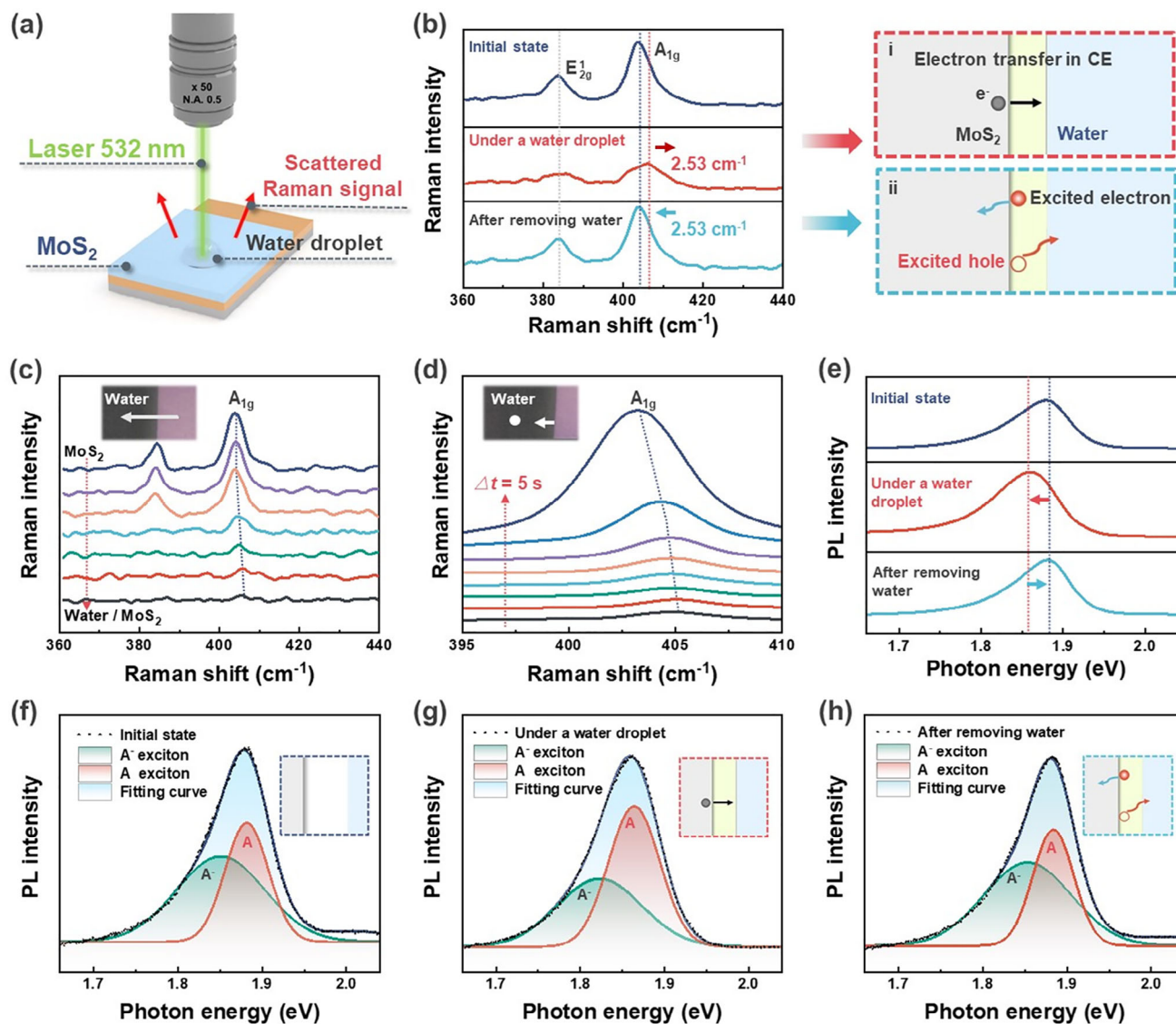


Figure 3. a) Schematic illustration of the Raman measurements. b) Raman spectra of ML-MoS₂ in three different states: at the initial state, under a water droplet, and after removing water. c) Line-scan Raman mapping crosses the water droplet boundary. Inset indicates Raman line scan direction. d) Time-resolved Raman spectra. Inset demonstrates the measure point and the water retraction direction. e) PL spectra in the three different states. f–h) Gaussian fits of the PL intensities for the A⁻ and A exciton peaks at the initial state, under a water droplet, and after removing water, respectively. Insets illustrate the electron transfer directions in different states of the tribovoltaic effect.

isolating water-induced electronic structure perturbations from positional artifacts. Raman and PL spectra of ML-MoS₂ were systematically acquired under three interfacial states: at the initial state, under a DI water droplet, and after removing water. This spectral comparison enables direct correlation between interfacial charge redistribution (electron transfer) and optoelectronic property modulation, bypassing indirect electrical signal interpretations.

Primarily, Raman spectral analysis reveals direct evidence of interfacial electron transfer through the A_{1g} mode, which exhibits high sensitivity to electronic perturbations.^[39,40] Figure 3b demonstrates a shift of 2.53 cm⁻¹ in the A_{1g} mode toward higher wave number under DI water exposure compared to its initial stage, directly evidencing interfacial charge transfer occurs.

Specifically, the right shift represents N-type doping in MoS₂ weakens, inferring electron transfer from MoS₂ to the water side. This mechanism is attributed to CE: the collision interactions between water molecules and ML-MoS₂ surface atoms induce electron cloud overlap under liquid pressure, facilitating interfacial electron transfer from MoS₂ to water (Figure 3b-i). Crucially, the spectroscopic determination of electron transfer direction exhibits striking congruence with the polarity of the externally measured built-in electric field (Figure S7b, Supporting Information). These dual independent evidentiary lines provide closed-loop verification for electron transfer in the CE process, validating the pre-established tribovoltaic effect model (Figure 2e).

After removing water, the A_{1g} mode shifts back to its initial position, suggesting the ML-MoS₂ film returns to its original

state. This left shift indicates interfacial electrons transfer back to the MoS₂ side during droplet detachment dynamics, corresponding to another type of electron transfer in the tribovoltaic effect (Figures 2f and 3b-ii): CE and bond interaction releases energy at the interface (bindington), exciting electron–hole pairs that undergo directional separation under the built-in electric field. Holes migrate to water, while electrons move to MoS₂, resulting in attenuation of the built-in electric field strength. Notably, the electron transfer direction aligns completely with the external positive short-circuit current (from water to MoS₂), which has been observed in prior experiments (Figure 2a,c). Here, the spectroscopic signatures coupled with external circuit measurements conclusively demonstrate the bindington-driven electron behavior.

These presented experiments systematically address two fundamental electron transfer modalities in the tribovoltaic effect: electrons transfer from MoS₂ to water due to CE; bindington-excited electrons separate to MoS₂, generating detectable charge flow in the external circuit. Here, systematic analyses combining spectroscopic evolution, external circuit PN junction characterization, and output electrical signal measurements collectively demonstrate the coexistence of dual charge transfer processes, constituting the complete working mechanism of the tribovoltaic effect. These findings provide comprehensive experimental validation of the previously proposed tribovoltaic effect model (Figure 2d–f).^[23–27]

To provide complementary characterization, Raman spectroscopy in line scan mode (Figure 3c) was conducted along the white line shown in the inset of Figures 3c and S9a (Supporting Information). The corresponding peak position change of the A_{1g} mode was summarized in Figure S9b (Supporting Information). With the test spot going deeper into the water area, a significant right shift of the A_{1g} mode was observed, further confirming interfacial electron transfer due to CE. Moreover, to resolve temporal dynamics, we constructed a continuously varying water–MoS₂ interface by promoting water evaporation. Raman measurements were repeated on the same spot every 5 s (the inset of Figure 3d), as the water droplet evaporated and the liquid–solid interface retracted. As shown in Figure 3d, the A_{1g} mode clearly shifts to the lower wave number, indicating the ML–MoS₂ film returns to its pristine state as the liquid interface retracts. The corresponding peak position change of the A_{1g} mode was summarized in Figure S9c (Supporting Information). This trend further confirms that the interfacial electron–hole pairs, which are excited by bindingtons, separates and then weakens the built-in electric field. These spatially and temporally resolved spectroscopic datasets establish a cause-effect chain, providing strong experimental evidence for the tribovoltaic effect model described in Figure 2d–f (Supporting Information).

Besides the Raman spectroscopy, PL spectroscopy was also employed to provide complementary evidence for interfacial charge dynamics from another perspective. As shown in Figure 3e, upon water contact, the PL peak position moves left and the intensity increases. This result corresponds to the PL peak shift observed when positive bias of 0.2–0.7 V is applied to the MoS₂ film (without water), which is shown in Figure S10a (Supporting Information). This means that the introduction of a water droplet is analogous to applying positive bias, resulting in weakening of N-type doping and reduction of electron density in MoS₂. This trend de-

livers additional verification for interfacial electron transfer from MoS₂ to water due to CE and formation of the built-in electric field.

Furthermore, the PL intensities of the A[−] and A exciton peaks were fitted with a Gaussian function, and the fitting results for the three different states are shown in Figure 3f–h. Figure S10b (Supporting Information) summarizes the relative intensity changes of the two excitons. In the initial state (Figure 3f), the intensity of the A[−] exciton is comparable to that of the A exciton. When water comes into contact with ML–MoS₂ (Figure 3g), the relative intensity of the A[−] exciton manifests a 33% diminution (Figure S10b, Supporting Information), indicating a reduction of excess electrons in MoS₂ (Relevant quantitative analyses are provided in Note S2, Supporting Information). This trend also demonstrates electron transfer from MoS₂ to water caused by CE. Figure 3h shows the ML–MoS₂ film returns to the initial state after the water droplet leaves. This trend corresponds to the process in which bindington-excited electron–hole pairs separate at the interface during water droplet motion, with electrons migrating to MoS₂ and holes to water, resulting in positive current output in the external circuit. These above findings from PL analysis and Raman spectroscopy are all consistent with the external electrical measurements, collectively illustrating the complete process of interfacial electron transfer in the liquid–solid tribovoltaic effect (Figure 2d–f), including both CE-induced electron transfer and bindington-excited electron transfer.

2.4. MD Simulations of the Water–MoS₂ Interface

While Raman and PL spectroscopies have demonstrated interfacial charge transfer during a water droplet contacts the ML–MoS₂ surface, but details of liquid–solid interactions still need to be further clarified. To address this, we used MD simulations using the LAMMPS software package. The ML–MoS₂ sheet was modeled by using the Stillinger–Weber (SW) potential,^[46] with periodic boundary conditions applied in the *x*- and *y*-directions. Thermostat and ensemble approach used in MD simulation is provided in the Experimental Section.

As depicted in Figure 4a, the water droplet on the MoS₂ surface was categorized into three distinct regions: region I (air-adjacent, 10 Å thickness), region II (>10 Å from air and >6 Å from MoS₂), and region III (<6 Å from MoS₂). By calculating the density distribution of oxygen atoms along the *z*-axis (perpendicular to the MoS₂ plane), Figure 4b shows an orderly accumulation of water molecules near the MoS₂ surface, while a decrease in density from the interface. Figure 4c quantifies the water molecule numbers in the three regions respectively. In Figure 4d, the numbers of hydrogen bonds (HBs) in different regions are calculated, and the average number of HBs per water molecule is provided in Figure 4e. The average number of HBs in region II is greater than that in the other two regions, illustrating other phases destroy the HB network of bulk water. Specifically, the reduced HB number at the interface indicates enhanced water molecular freedom, facilitating their active participation in electron transfer processes.

Angular distributions of O–H bonds of water molecules relative to the *z*-axis were analyzed for regions II and III (Figure 4f,g). Water molecules in region II show isotropic orientation, while

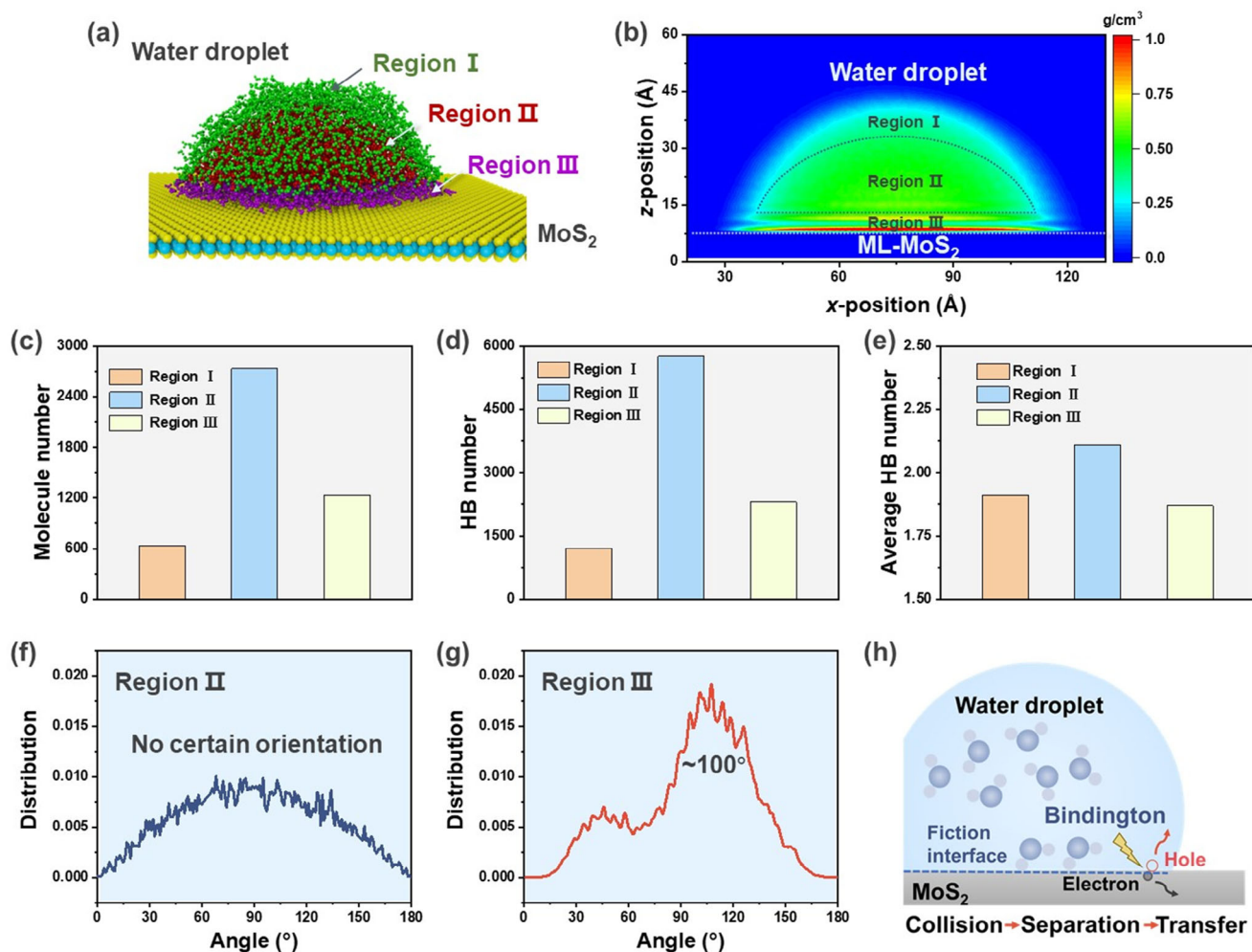


Figure 4. a) Schematic illustration showing the three defined regions within a water droplet on the ML-MoS₂ surface. b) Normalized density profile of oxygen atoms in water molecules along the z-axis. c) Number of water molecules in each region. d) Number of HBs formed in each region. e) Average number of HBs per water molecule in each region. f,g) Probability distributions of the angles of the O–H bonds relative to the z-axis for region II and region III. h) Diagram illustrating the tribovoltaic effect at the MoS₂–water interface.

those in region III exhibit distinct angular preferences with peaks near 40° and 100°. Combined with the HB characteristics in region III, this bimodal distribution suggests interfacial water molecules adopt a specific configuration: one O–H bond is nearly parallel to the MoS₂ surface, and the other protrudes as a surface-directed “dangling” bond, as depicted in Figure S11 (Supporting Information). These structural details provide molecular-level insights into the tribovoltaic effect at the dynamic liquid–solid interface (Figure 4h): the dangling O–H bonds interacts with the ML-MoS₂ surface continuously, releasing bindingtons to excite electron–hole pairs and output DC electrical signals in the external circuit.

Unlike the photovoltaic effect, the energy available to excite electron–hole pairs at the interfaces in the tribovoltaic effect originates from friction. Considering the tribovoltaic effect can also occur at super-lubricated interfaces, the generation of electron–hole pairs is not attributed to material deformation caused by macroscopic friction. Instead, phonons can be generally excited at the interface during material sliding, resulting from local elas-

tic and plastic deformation. However, phonons typically carry energy in the range of 10–50 meV,^[24] which is insufficient to excite electron–hole pairs in a PN junction. Consequently, the energy dissipation during friction must be examined at the atomic scale. In various microfriction models, energy is dissipated in the forms of atomic vibrations and chemical bond formation, with bond formation releasing energy that can be substantial enough to excite electron–hole pairs. For instance, during silicon wafer sliding, silanol condensation reactions occur between dangling –OH groups on silicon atoms, leading to the formation of siloxane bonds.^[24] The formation of these chemical bonds releases energy quantum, which is referred to as bindington. The energy value of bindington depends on the energy difference between the orbitals of the electron before and after bonding, estimated to be the order of several electron volts.^[24] This energy level is sufficient to excite an electron–hole pair at least at the semiconductor interface, so the chemical bond formation should be a crucial energy source for the excitation of electrons. Nevertheless, the complexity of friction process, particularly liquid–solid

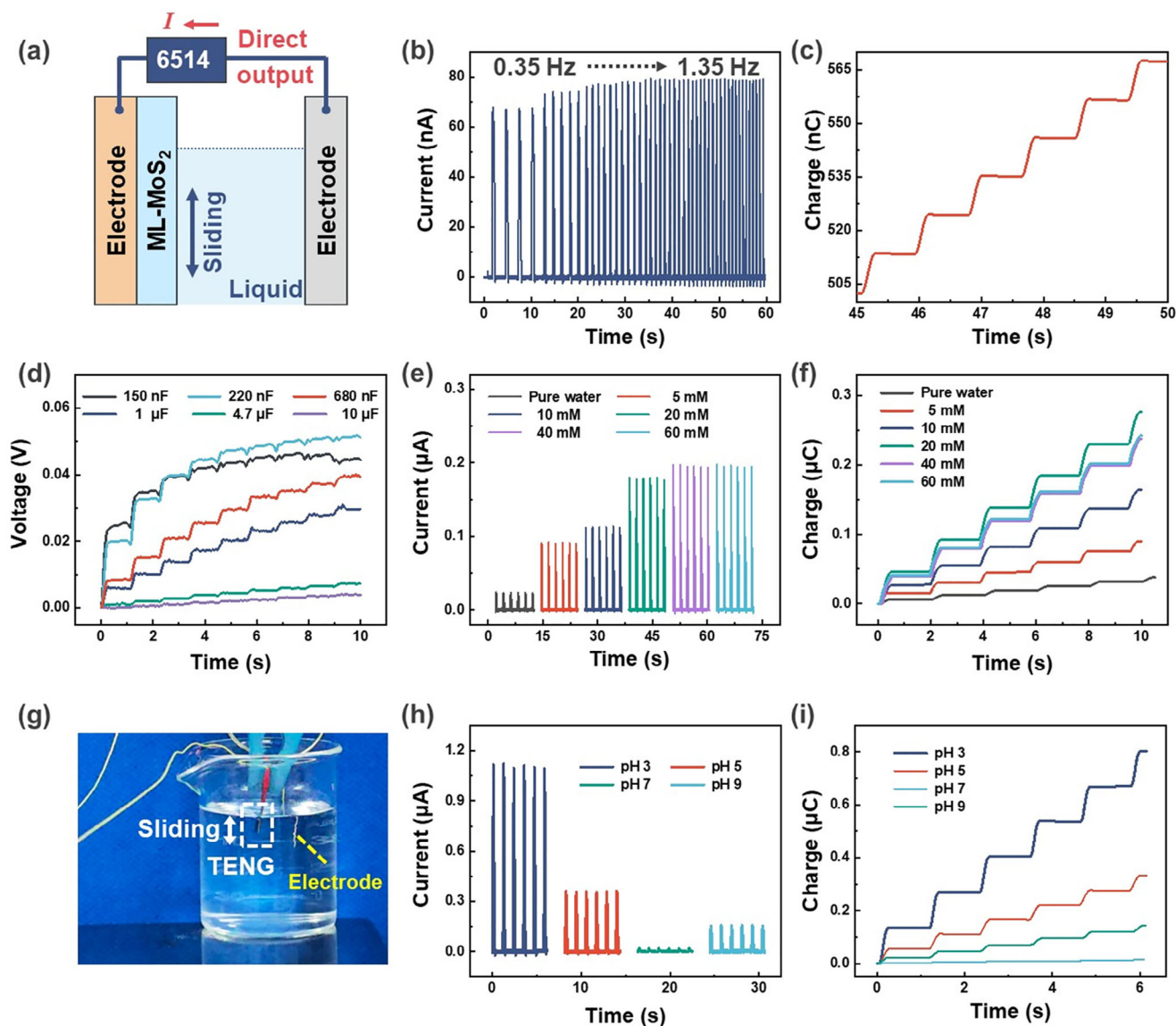


Figure 5. a) Schematic of the test environment. b) Output current as the motion frequency increases from 0.35 to 1.35 Hz. c) Transferred charge over 5 s. d) Voltage curves of a series of capacitors (ranging from 150 nF to 10 μ F) charged by the nanogenerator. e) Output current and f) transferred charge of the nanogenerator working in NaCl solutions with varying concentrations. g) Photograph of the nanogenerator in operation. h) Output current and i) transferred charge of the nanogenerator working in solutions with different pH values.

interactions, requires further investigation to fully elucidate the underlying processes in future research.

2.5. Influences of Different Solutions on the Output Performance

The above experiments demonstrate that MoS₂ can serve as an effect tribomaterial for liquid–solid nanogenerators. To further evaluate its output performance, we designed a reciprocating motor to drive the nanogenerator vertically in a water tank, as illustrated in Figure 5a. The photograph of the working environment is exhibited in Figure 5g. Video S2 (Supporting Information) captures the working process and directly visualizes real-time charge accumulation during operation. As shown in Figure 5b, the out-

put current increases from 67.47 to 78.86 nA as the working frequency rises from 0.35 to 1.35 Hz. The detailed relationship between output current and frequency is summarized in Figure S12a (Supporting Information). At the frequency of 1.0 Hz, the current reaches 78.82 nA. Beyond this point, higher frequency has only a minor influence on the current. The corresponding transferred charge is partly shown in Figure 5c, and the transferred charge of 65.24 nC is achieved within 5 s. For the output voltage, the maximum voltage peak is about 0.2 V, which is a result after filtering, as shown in Figure S12b (Supporting Information). In order to investigate the charging capability of the nanogenerator, we measured a series of voltage curves when charging capacitors from 150 nF to 10 μ F over 10 s (Figure 5d). Unfortunately, since the output voltage is too low, charges cannot

be effectively injected into the capacitors. In order to illustrate the stability and durability of the nanogenerator, repeated output measurements were conducted under consistent testing conditions (Figure S13, Supporting Information). Subjected to contact with DI water at a frequency of 0.71 Hz, the output current was recorded at three time points: 0, 24, and 48 h. The current values consistently remain across all measurements, with no significant degradation or variation observed. Even after extended operation, the device maintains high reliability in performance.

Next, we explored the output performances of the nanogenerator working in different solutions. Figure 5e,f shows the device performances working in NaCl solutions with varying concentrations. As the salinity increases from 0 to 60×10^{-3} mM (mmol L^{-1}), both the output current and transferred charge increase. Figure S14a (Supporting Information) shows the I - V curves are not obviously influenced by different salinities, implying the same built-in electric field. Therefore, the increasing trend can be attributed to the enhanced conductivity. However, nonlinear growth trajectory suggests saturation effects emerge at higher salinities due to finite binding site availability and interfacial electron-hole pair generation capacity. On the other hand, the effect of pH on output performances was also discussed, as shown in Figure 5h,i. At $\text{pH} = 3$, the output current reaches the maximum of 1.11 μA , and the current density is 11.1 mA m^{-2} . The I - V curves with different pH values are provided in Figure S14b (Supporting Information), all of which demonstrate the same direction of rectification. The comparison of the output level with other liquid-solid TENGs using different solid surfaces, including MoS_2 , Si, graphene, and PTFE can be found in Note S3 (Supporting Information).^[6,26,47,48] In IoT applications, the current density of 11.1 mA m^{-2} may be useful in specific scenarios, such as sensor nodes, smart networks, wearable devices, and environmental monitoring. However, due to the relatively low output voltage (at the mV level), further efforts must focus on the development of effective unit circuit integration strategies to enhance the performance of the system. Moreover, the optimization methods for the tribovoltaic effect are discussed in Note S4 (Supporting Information).

3. Conclusion

This study establishes a DC liquid-solid nanogenerator using 2D semiconductor ML- MoS_2 to investigate interfacial charge transfer mechanisms. First, by manipulating DI water droplets on MoS_2 surfaces via a microinjector, we confirmed DC tribovoltaic output characteristics through external circuit signals. Next, Raman and PL spectroscopy analyses revealed electron transfer dynamics at the liquid-solid interface, supported by MD simulations clarifying interaction details. Integrated experimental and theoretical approaches advanced understanding of liquid-solid CE and the tribovoltaic effect. Finally, testing demonstrated salinity/pH-dependent output performances, and the output current reached the maximum of 1.11 μA at $\text{pH} = 3$. In conclusion, this work not only pioneers ML- MoS_2 as a tribomaterial for DC liquid-solid nanogenerators, but also establishes a foundational framework for the liquid-solid tribovoltaic effect research, highlighting promising pathways for micro-nano energy harvesting applications.

4. Experimental Section

Sample Preparation: The ML- MoS_2 sample ($1 \text{ cm} \times 1 \text{ cm}$) was provided by SixCarbon technology, Shenzhen. The ML- MoS_2 was transferred onto a silicon wafer ($1.5 \text{ cm} \times 1 \text{ cm}$) coated with a 100-nm-thick Cu electrode by using the polymethyl methacrylate (PMMA) layer-assisted transfer method. The surface morphology of the samples was characterized by SEM (TESCAN MIRA LMS) and AFM (Park XE-100). The contact angles of the film and water were acquired by a contact angle measuring machine (SDC350KS).

Electrical Measurements: The DI water used here was produced by deionizer (ELGA), and the resistivity of the DI water was $18.2 \text{ M}\Omega \text{ cm}$. A 25 μL microinjector was applied to manipulate the volume of the DI water droplet. The electrical signals between the conductive needle of the microinjector and the back electrode were measured by a Keithley 6514 System Electrometer equipped with a current preamplifier.

Current–Voltage Measurements: The I - V curves were obtained using a Keithley 4200A-SCS semiconductor parameter analyzer. The voltage scan interval was set to 0.01 V.

Raman and PL Measurements: All experiments were conducted at room temperature using a 532 nm laser with a power setting of 10%. For the Raman spectroscopy, a 2400 lines mm^{-1} grating was employed, while a 1200 lines mm^{-1} grating was used for PL measurements. A $50 \times$ objective lens with a short working distance was utilized for laser focusing and signal collection, ensuring precise focus on the MoS_2 sample. Prior to measurements, the Raman spectrometer was calibrated using a silicon wafer with a characteristic Raman peak at 520.7 cm^{-1} .

MD Simulations: MD simulations with 2 000 000 timesteps were performed at the temperature of 300 K under NVT ensemble (constant particle number, constant volume, and constant temperature) to investigate the structural properties of a water droplet. Temperature control was maintained using the Nosé–Hoover thermostat. MD box with dimensions of $150 \text{ \AA} \times 150 \text{ \AA} \times 80 \text{ \AA}$ was generated. The ML- MoS_2 sheet with 2D dimensions of $150 \text{ \AA} \times 150 \text{ \AA}$ was placed at the bottom region, and a cubic water droplet with dimensions of $70 \text{ \AA} \times 70 \text{ \AA} \times 70 \text{ \AA}$ was placed above it. The MoS_2 sheet was composed of 2538 and 5076 Mo and S atoms, while the water droplet consists of 5000 water molecules. No atoms were removed or introduced during the simulation, ensuring that the number of particles remains constant. The x - and y -directions employed periodic boundary conditions, allowing for volume fluctuations, while the z -direction was fixed. With the z -direction fixed, the total volume can be regarded as approximately constant. The model was developed by incorporating insights from the work of Sose et al.^[46]

Device Performance Measurements: To evaluate the output performances under various solutions, a self-designed reciprocating motor was employed to drive the nanogenerator to contact the liquid periodically at a fixed frequency. The pH of the solutions was precisely adjusted by HCl and NaOH to ensure controlled acidic or alkaline conditions. The output voltage, current, transferred charge, and charging performance were all measured using a Keithley 6514 System Electrometer equipped with a current preamplifier.

Supporting Information

Supporting Information is available from the Wiley Online Library or from the author.

Acknowledgements

Supports from R&D program of Beijing Municipal Education Commission (KM202410028019), Natural Science Foundation for Youths of Inner Mongolia Autonomous Region (No. 2025QN01020), and Inner Mongolia University of Science and Technology Keju Talent Reserve Program (No. KJJH2024956) are appreciated.

Conflict of Interest

The authors declare no conflict of interest.

Author Contributions

X.L. conceived and planned this work. Y.X. conducted the experiments. Q.Y., W.B., and P.W. handled the spectroscopic analysis. M.Z. and T.J. provided the conceptual framework for the manuscript writing. Z.L.W. supervised the work. All co-authors took part in discussion of the results and writing manuscript.

Data Availability Statement

The data that support the findings of this study are available from the corresponding author upon reasonable request.

Keywords

charge transfer, contact electrification, liquid–solid interface, ML-MoS₂, spectral analysis, triboelectric nanogenerator, tribovoltaic effect

Received: April 1, 2025

Revised: June 10, 2025

Published online:

- [1] T. Zhao, M. Xu, X. Xiao, Y. Ma, Z. Li, Z. L. Wang, *Nano Energy* **2021**, *88*, 106199.
- [2] Z. L. Wang, *Nature* **2017**, *542*, 159.
- [3] Z. L. Wang, T. Jiang, L. Xu, *Nano Energy* **2017**, *39*, 9.
- [4] J. Tan, X. Wang, W. Chu, S. Fang, C. Zheng, M. Xue, X. Wang, T. Hu, W. Guo, *Adv. Mater.* **2024**, *36*, 2211165.
- [5] Y. Li, X. Liu, Z. Ren, J. Luo, C. Zhang, C. Cao, H. Yuan, Y. Pang, *Nano Energy* **2024**, *119*, 109046.
- [6] Z. H. Lin, G. Cheng, S. Lee, Z. L. Wang, *Adv. Mater.* **2014**, *26*, 4690.
- [7] G. Zhu, Y. Su, P. Bai, J. Chen, Q. Jing, W. Yang, Z. L. Wang, *ACS Nano* **2014**, *8*, 6031.
- [8] W. Xu, Q. Chen, Q. Ren, J. Li, Q. Chen, C. Zhu, Y. Xie, W. Li, *Nano Energy* **2024**, *131*, 110191.
- [9] C. Ye, D. Liu, P. Chen, L. N. Y. Cao, X. Li, T. Jiang, Z. L. Wang, *Adv. Mater.* **2023**, *35*, 2209713.
- [10] Y. Zhang, Y. Li, R. Cheng, S. Shen, J. Yi, X. Peng, C. Ning, K. Dong, Z. L. Wang, *Research* **2022**, *2022*, 9809406.
- [11] W. Yuan, B. Zhang, C. Zhang, O. Yang, Y. Liu, L. He, L. Zhou, Z. Zhao, J. Wang, Z. L. Wang, *One Earth* **2022**, *5*, 1055.
- [12] Y. Li, S. Chen, H. Yan, H. Jiang, J. Luo, C. Zhang, Y. Pang, Y. Tan, *Chem. Eng. J.* **2023**, *468*, 143572.
- [13] Y. Pang, Y. Fang, J. Su, H. Wang, Y. Tan, C. Cao, *Adv. Mater. Technol.* **2023**, *8*, 2201246.
- [14] W. Xu, H. Zheng, Y. Liu, X. Zhou, C. Zhang, Y. Song, X. Deng, M. Leung, Z. Yang, R. X. Xu, Z. L. Wang, X. C. Zeng, Z. Wang, *Nature* **2020**, *578*, 392.
- [15] B. Zhang, J. Li, J. Zhou, L. Chow, G. Zhao, Y. Huang, Z. Ma, Q. Zhang, Y. Yang, C. K. Yiu, J. Li, F. Chun, X. Huang, Y. Gao, P. Wu, S. Jia, H. Li, D. Li, Y. Liu, K. Yao, R. Shi, Z. Chen, B. L. Khoo, W. Yang, F. Wang, Z. Zheng, Z. Wang, X. Yu, *Nature* **2024**, *628*, 84.
- [16] Y. Li, X. Qin, Y. Feng, Y. Song, Z. Yi, H. Zheng, P. Zhou, C. Wu, S. Yang, L. Wang, P. Zhu, W. Xu, Z. Wang, *Droplet* **2024**, *3*, 91.
- [17] J. Hu, M. Iwamoto, X. Chen, *Nano-Micro Lett.* **2024**, *16*, 7.
- [18] X. Wei, B. Wang, X. Cao, H. Zhou, Z. Wu, Z. L. Wang, *Nat. Food* **2023**, *4*, 721.
- [19] H. Zou, L. Guo, H. Xue, Y. Zhang, X. Shen, X. Liu, P. Wang, X. He, G. Dai, P. Jiang, H. Zheng, B. Zhang, C. Xu, Z. L. Wang, *Nat. Commun.* **2020**, *11*, 2093.
- [20] F. Xi, Y. Pang, W. Li, T. Jiang, L. Zhang, T. Guo, G. Liu, C. Zhang, Z. L. Wang, *Nano Energy* **2017**, *37*, 168.
- [21] H. Zhang, F. Marty, X. Xia, Y. Zi, T. Bourouina, D. Galayko, P. Basset, *Nat. Commun.* **2020**, *11*, 3221.
- [22] H. Zhou, G. Liu, J. Zeng, Y. Dai, W. Zhou, C. Xiao, T. Dang, W. Yu, Y. Chen, C. Zhang, *Sensors* **2022**, *22*, 1668.
- [23] Z. L. Wang, A. C. Wang, *Mater. Today* **2019**, *30*, 34.
- [24] S. Lin, Z. L. Wang, *Mater. Today* **2023**, *62*, 111.
- [25] X. Xu, Z. L. Wang, Z. Yang, *Energy Environ. Sci.* **2024**, *17*, 149.
- [26] S. Lin, X. Chen, Z. L. Wang, *Nano Energy* **2020**, *76*, 105070.
- [27] Y. Yan, X. Zhou, S. Feng, Y. Lu, J. Qian, P. Zhang, X. Yu, Y. Zheng, F. Wang, K. Liu, S. Lin, *J. Phys. Chem. C* **2021**, *125*, 14180.
- [28] M. Zheng, S. Lin, Z. Tang, Y. Feng, Z. L. Wang, *Nano Energy* **2021**, *83*, 105810.
- [29] M. Zheng, S. Lin, L. Zhu, Z. Tang, Z. L. Wang, *Adv. Mater. Interfaces* **2021**, *9*, 2101757.
- [30] X. Hu, H. Jiang, L. X. Lu, S. X. Zhao, Y. Li, L. Zhen, C. Y. Xu, *Small* **2023**, *19*, 2301798.
- [31] X. Li, R. Li, S. Li, Z. L. Wang, D. Wei, *Nat. Commun.* **2024**, *15*, 6182.
- [32] J. Zhang, X. Wang, L. Zhang, S. Lin, S. Ciampi, Z. L. Wang, *J. Am. Chem. Soc.* **2024**, *146*, 6125.
- [33] T. Wu, K. Liu, S. Liu, X. Feng, X. Wang, L. Wang, Y. Qin, Z. L. Wang, *Adv. Mater.* **2023**, *35*, 2208121.
- [34] W. Dong, Z. Dai, L. Liu, Z. Zhang, *Adv. Mater.* **2023**, *36*, 2303014.
- [35] J. Liu, A. Goswami, K. Jiang, F. Khan, S. Kim, R. McGee, Z. Li, Z. Hu, J. Lee, T. Thundat, *Nat. Nanotechnol.* **2017**, *13*, 112.
- [36] J. Liu, F. Liu, R. Bao, K. Jiang, F. Khan, Z. Li, H. Peng, J. Chen, A. Alodhayb, T. Thundat, *ACS Appl. Mater. Interfaces* **2019**, *11*, 35404.
- [37] Q. H. Wang, K. K. Zadeh, A. Kis, J. N. Coleman, M. S. Strano, *Nat. Nanotechnol.* **2012**, *7*, 699.
- [38] I. Kylänpää, H. P. Komsa, *Phys. Rev. B* **2015**, *92*, 205418.
- [39] T. Sohier, E. Ponomarev, M. Gibertini, H. Berger, N. Marzari, N. Ubrig, A. F. Morpurgo, *Phys. Rev. X* **2019**, *9*, 031019.
- [40] Y. Li, C. Y. Xu, J. K. Qin, W. Feng, J. Y. Wang, S. Zhang, L. P. Ma, J. Cao, P. A. Hu, W. Ren, L. Zhen, *Adv. Funct. Mater.* **2015**, *26*, 293.
- [41] C. Zhu, P. Liu, B. Niu, Y. Liu, W. Xin, W. Chen, X. Y. Kong, Z. Zhang, L. Jiang, L. Wen, *J. Am. Chem. Soc.* **2021**, *143*, 1932.
- [42] Y. Han, D. Liu, *Nano Res.* **2024**, *17*, 7513.
- [43] H. Zhong, F. Pan, S. Yue, C. Qin, V. Hadjiev, F. Tian, X. Liu, F. Lin, Z. Wang, Z. Ren, J. Bao, *J. Phys. Chem. Lett.* **2023**, *14*, 6702.
- [44] Z. Tang, Y. Dan, H. Guo, S. Lin, Z. L. Wang, *Adv. Mater.* **2024**, *36*, 2400451.
- [45] S. Lin, L. Xu, A. Chi Wang, Z. L. Wang, *Nat. Commun.* **2020**, *11*, 399.
- [46] A. T. Sose, E. Mohammadi, P. F. Achari, S. A. Deshmukh, *J. Phys. Chem. C* **2022**, *126*, 2013.
- [47] S. Aji, R. Nishi, H. Ago, Y. Ohno, *Nano Energy* **2020**, *68*, 104370.
- [48] J. Yin, X. Li, J. Yu, Z. Zhang, J. Zhou, W. Guo, *Nat. Nanotechnol.* **2014**, *9*, 378.